# 2

# Atomic Force Microscopy in Optical Imaging and Characterization

Martin Veis[1] and Roman Antos[2]
[1]*Institute of Physics, Faculty of Mathematics and Physics, Charles University*
*Institute of Biophysics and Informatics, 1st Faculty of Medicine, Charles University*
[2]*Institute of Physics, Faculty of Mathematics and Physics, Charles University*
*Czech Republic*

## 1. Introduction

Atomic force microscopy (AFM) is a state of the art imaging system that uses a sharp probe to scan backwards and forwards over the surface of an object. The probe tip can have atomic dimensions, meaning that AFM can image the surface of an object at near atomic resolution. Two big advantages of AFM compared to other methods (for example scanning tunneling microscopy) are: the samples in AFM measurements do not need to be conducting because the AFM tip responds to interatomic forces, a cumulative effect of all electrons instead of tunneling current, and AFM can operate at much higher distance from the surface (5-15 nm), preventing damage to sensitive surfaces.

An exciting and promising area of growth for AFM has been in its combination with optical microscopy. Although the new optical techniques developed in the past few years have begun to push traditional limits, the lateral and axial resolution of optical microscopes are typically limited by the optical elements in the microscope, as well as the Rayleigh diffraction limit of light. In order to investigate the properties of nanostructures, such as shape and size, their chemical composition, molecular structure, as well as their dynamic properties, microscopes with high spatial resolution as well as high spectral and temporal resolving power are required. Near-field optical microscopy has proved to be a very promising technique, which can be applied to a large variety of problems in physics, chemistry, and biology. Several methods have been presented to merge the optical information of near-field optical microscopy with the measured surface topography. It was shown by (Mertz et al. (1994)) that standard AFM probes can be used for near-field light imaging as an alternative to tapered optical fibers and photomultipliers. It is possible to use the microfabricated piezoresistive AFM cantilevers as miniaturized photosensitive elements and probes. This allows a high lateral resolution of AFM to be combined with near-field optical measurements in a very convenient way. However, to successfully employ AFM techniques into the near-field optical microscopy, several technical difficulties have to be overcome.

Artificial periodical nanostructures such as gratings or photonics crystals are promising candidates for new generation of devices in integrated optics. Precise characterization of their lateral profile is necessary to control the lithography processing. However, the limitation of AFM is that the needle has to be held by a mechanical arm or cantilever. This restricts

the access to the sample and prevents the probing of deep channels or any surface that isn't predominantly horizontal. Therefore to overcome these limitations the combination of AFM and optical scatterometry which is a method of determining geometrical (and/or material) parameters of patterned periodic structures by comparing optical measurements with simulations, the least square method and a fitting procedure is used.

## 2. AFM probes in near-field optical microscopy

In this section we review two experimental approaches of the near-field microscopy that use AFM tips as probing tools. The unique geometrical properties of AFM tips along with the possibility to bring the tip apex close to the sample surface allow optical resolutions of such systems to few tens of nanometers. These resolutions are not reachable by conventional microscopic techniques. For readers who are interested in the complex near-field optical phenomena we kindly recommend the book of (Novotny & Hecht (2006)).

### 2.1 Scattering-type scanning near-field optical microscopy

Scanning near field optical microscopy (SNOM) is a powerful microscopic method with an optical resolution bellow the Rayleigh diffraction limit. The optical microscope can be setup as either an aperture or an apertureless microscope. An aperture SNOM (schematically shown in Fig. 1(a)) uses a metal coated dielectric probe, such as tapered optical fibre, with a submicrometric aperture of diameter $d$ at the apex. For the proper function of such probe it is necessary that $d$ is above the critical cutoff diameter $d_c = 0.6\lambda/n$, otherwise the light propagation becomes evanescent which results in drastic $\lambda$ dependent loss (Jackson (1975)). This cutoff effect significantly limits the resolution which can be achieved. The maximal resolution is therefore limited by the minimal aperture $d \approx \lambda/10$. In the visible region the 50 nm resolution is practically achievable (Hecht (1997)). With the increasing wavelength of illumination light, however, the resolution is decreased. This leads to the maximum resolution of $1\mu m$ in mid-infrared region, which is non usable for microscopy of nanostructures.

To overcome the limitations of aperture SNOM, one can use a different source of near field instead of the small aperture. This source can be a small scatter, such as nanoscopic particle or sharp tip, illuminated by a laser beam. When illuminated, these nanostructures provide an enhancement of optical fields in the proximity of their surface. This is due to a dipole in the tip which is induced by the illumination beam. This dipole itself induces a mirror dipole in the sample when the tip is brought very closely to its surface. Owing to this near-field interaction, complete information about the sample's local optical properties is determined by the elastically scattered light (scattered by the effective dipole emerging from the combination of tip and sample dipoles) which can be detected in the far field using common detectors. This is a basis of the scattering-type scanning near-field optical microscope (s-SNOM). There are two observables of practical importance in the detected signal: The absolute scattering efficiency and the material contrast (the relative signal change when probing nanostructures made from different materials). The detection of scattered radiation was first demonstrated in the microwave region by (Fee et al. (1989)) (although the radiation was confined in waveguide) and later demonstrated at optical frequencies by using an AFM tip as a scatterer (Zenhausern et al. (1995)) The principle of s-SNOM is shown in Figure 1(b). Both the optical and mechanical resolutions are determined by the radius of curvature $a$ at the tip's apex and the optical resolution is independent of the wavelength of the illumination beam. To theoretically solve the complex problem of the realistic scattering of the illuminating light by an elongated tip in

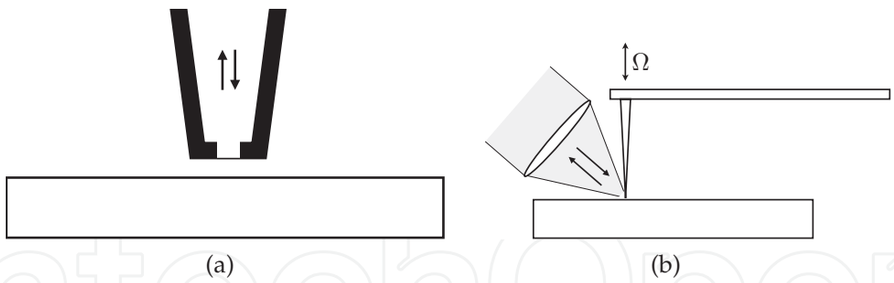


Fig. 1. Principles of aperture (a) and apertureless (b) scanning near-field optical microscopies.

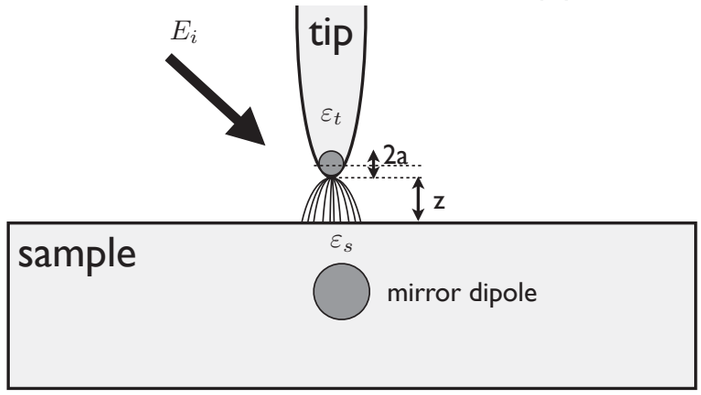


Fig. 2. Schematic view of the simplified theoretical geometry, where the tip was replaced by a small sphere at the tips apex. The sample response is characterized by an induced mirror dipole.

the proximity of the sample's surface it is necessary to use advanced electromagnetic theory, which is far beyond the scope of this chapter (readers are kindly referred to the work of (Porto et al. (2000))). However (Knoll & Keilmann (1999b)) demonstrated that the theoretical treatment based on simplified geometry can be used for quantitative calculation of the relative scattering when probing different materials. They have approximated the elongated probe tip by a polarizable sphere with dielectric constant $\varepsilon_t$, radius $a$ ($a \ll \lambda$) and polarizability (Zayats & Richards (2009))

$$\alpha = 4\pi a^3 \frac{(\varepsilon_t - 1)}{(\varepsilon_t + 2)}. \tag{1}$$

This simplified geometry is schematically shown in Figure 2. The dipole is induced by an incident field $E_i$ which is polarized parallel with the tip's axis ($z$ direction). The incident polarization must have the $z$ component. In this case the tip's shaft acts as an antenna resulting in an enhanced near-field (the influence of the incident polarization on the near-field enhancement was investigated by (Knoll & Keilmann (1999a))). This enhanced field exceeds the incident field $E_i$ resulting in the indirect polarization of the sample with dielectric constant $\varepsilon_s$, which fills the half-space $z < 0$. Direct polarization of the sample by $E_i$ is not assumed.

To obtain the polarization induced in the sample, the calculation is approximated by assuming the dipole as a point in the centre of the sphere. Then the near-field interaction between the tip dipole and the sample dipole in the electrostatic approximation can be described by the polarizability $\alpha\beta$ where

$$\beta = \frac{(\varepsilon_s - 1)}{(\varepsilon_s + 1)} \tag{2}$$

Note that the sample dipole is in the direction parallel to those in the tip and the dipole field is decreasing with the third power of the distance. Since the signal measured on the detector is created by the light scattered on the effective sample-tip dipole, it is convenient to describe the near-field interaction by the combined effective polarizability as was done by (Knoll & Keilmann (1999b)). This polarizability can be expressed as

$$\alpha_{\text{eff}} = \frac{\alpha(1+\beta)}{1 - \frac{\alpha\beta}{16\pi(a+z)^3}}, \tag{3}$$

where $z$ is the gap width between the tip and the sample. For a small particle, the scattered field amplitude is proportional to the polarizability (Keilmann & Hillenbrand (2004))

$$E_s \propto \alpha_{\text{eff}} E_i. \tag{4}$$

Since the quantities $\varepsilon$, $\beta$ and $\alpha$ are complex, the effective polarizability can be generally characterized by a relative amplitude $s$ and phase shift $\varphi$ between the incident and the scattered light

$$\alpha_{\text{eff}} = s e^{i\varphi}. \tag{5}$$

The validity of the theoretical approach described above was determined by numerous s-SNOM studies published by (Hillenbrand & Keilmann (2002); Knoll & Keilmann (1999b); Ocelic & Hillenbrand (2004)). Good agreement between experimental and theoretical s-SNOM contrast was achieved.

Recalling the Equation (3) it is important to note that the change of the illumination wavelength will lead to changes in the scattering efficiency as the values of the dielectric constants $\varepsilon_s$ and $\varepsilon_t$ will follow dispersion relations of related materials. This allows to distinguish between different materials if the tip's response is flat in the spectral region of interest. Therefore the proper choice of the tip is important to enhance the material contrast and the resolution.

(Cvitkovic et al. (2007)) reformulated the coupled dipole problem and derived the formula for the scattered amplitude in slightly different form

$$E_s = (1+r)^2 \frac{\alpha(1+\beta)}{1 - \frac{\alpha\beta}{16\pi(a+z)^3}}. \tag{6}$$

They introduced Fresnel reflection coefficient of the flat sample surface. This is important to account for the extra illumination of the probe via reflection from the sample which was neglected in Equations (3) and (4).

The detected signal in s-SNOM is a mixture of the near-field scattering and the background scattering from the tip and the sample. Prior to the description of various experimental s-SNOM setups it is important to note how to eliminate the unwanted background scattering from the detector signal. For this purpose we have calculated the distance dependence of $\alpha_{\text{eff}}$. The result is displayed in Figure 3. As one can see from this figure, the scattering is almost constant for distances larger than $2a$. On the other hand for very short distances (very closely to the sample) both the scattering amplitude and the scattering phase drastically increase. This

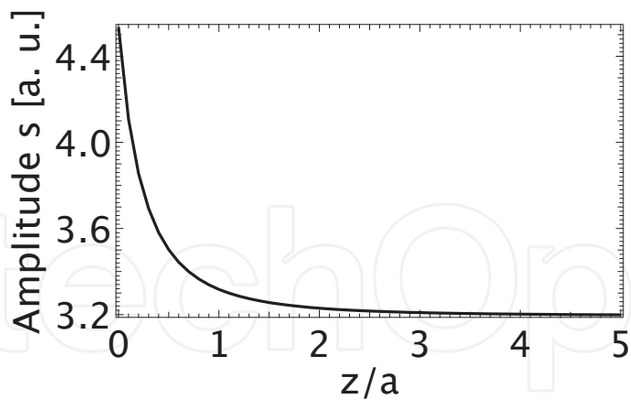


(a)

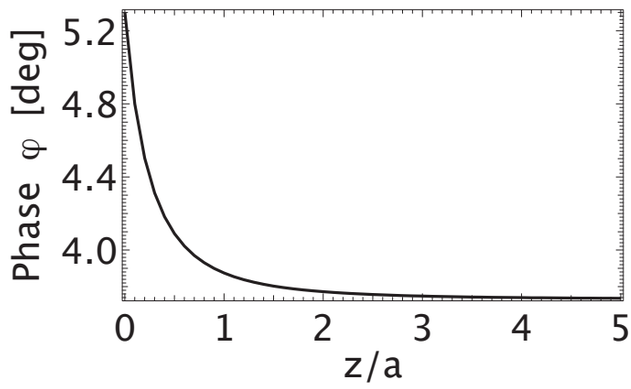


(b)

Fig. 3. Theoretically calculated dependence of the near-field scattering amplitude $s$ (a) and phase $\varphi$ (b) on the tip-sample distance $z$.

occurs for various materials with various dielectric constants demonstrating the near-field interaction.

When the tip is illuminated by a focused laser beam, only a small portion of the incident light reaches the gap between the tip and the sample and contributes to the near-field. Therefore the detected signal is mainly created by the background scattering. The nonlinear behavior of the $\alpha_{\mathrm{eff}}(z)$ is employed to filter out the unwanted background scattering which dominates in the detected signal. This can be done if one employs tapping mode with a tapping frequency $\Omega$ into the experimental setup. The tapping of amplitude $\Delta z \approx a \approx 20nm$ modulates the near-field scattering much stronger than the background scattering. The nonlinear dependence of $\alpha_{\mathrm{eff}}(z)$ will introduce higher harmonics in the detected signal. The full elimination of the background is done by demodulating the detector signal at the second or higher harmonic of $\Omega$ as was demonstrated by (Hillenbrand & Keilmann (2000)) and others.

There are various modifications of the s-SNOM experimental setup. Schematic views of interferometric s-SNOM experimental setups with heterodyne, homodyne and pseudohomodyne detection are displayed in Figure 4.

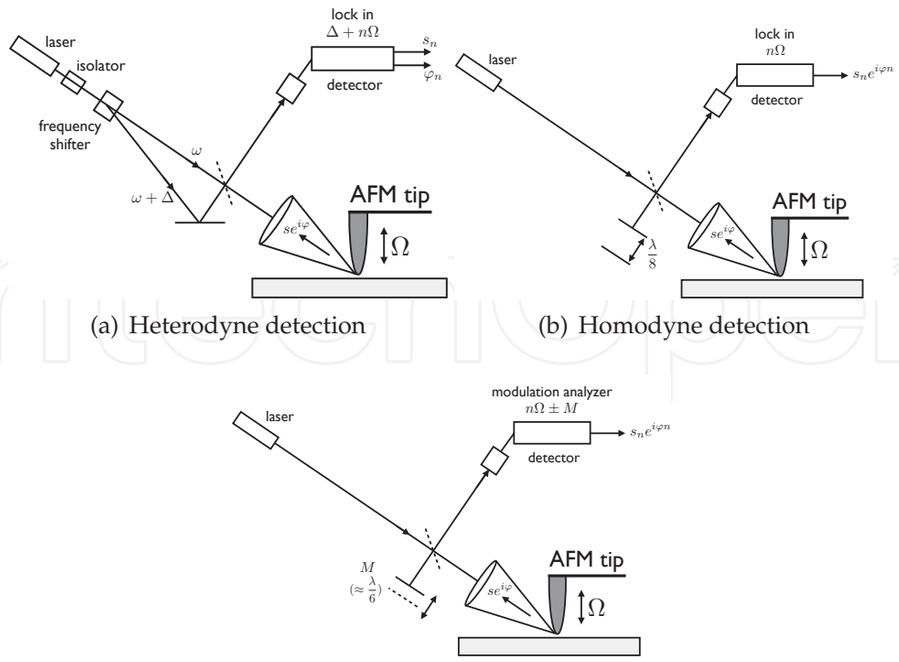


(a) Heterodyne detection (b) Homodyne detection

(c) Pseudo-homodyne detection

Fig. 4. Schematic views of experimental interferometric s-SNOM setups

The heterodyne detection system developed by (Hillenbrand & Keilmann (2000)) uses a HeNe laser with output power of $\approx$ 1mW as the illumination source. The beam passes through the optical isolator to filter the back reflections from the frequency shifter. The frequency shifter creates a reference beam with the frequency shifted by $\Delta = 80$MHz which interferes with the backscattered light from the sample in a heterodyne interferometer. The detected intensity is therefore $I = I_{ref} + I_s + 2\sqrt{I_{ref} I_s} \cos(\Delta t + \varphi)$. The signal is processed in high frequency lock-in amplifier which operates on the sum frequency $\Delta + n\Omega$. Here $n$ is the number of higher harmonic. The lock-in amplifier gives two output signals. One is proportional to scattering amplitude while the second is proportional to the phase of the detector modulation at frequency $\Delta + n\Omega$. When the order of harmonic $n$ is sufficiently large the signal on the lock-in amplifier is proportional to $s_n$ and $\varphi_n$. This means that using higher harmonics, one can measure pure near-field response directly. Moreover such experimental setup has optimized signal/noise ratio.

The influence of higher harmonic demodulation on the background filtering is demonstrated in Figure 5. In this figure the tip was used to investigate gold islands on Si substrate. For $n = 1$ the interference of different background contributions is clearly visible for $z > a$. Such interference may overlap with the important near-field interaction increase for $z < a$ which leads to a decrease of the contrast. Taking into account the second harmonic ($n = 2$) one can see a rapid decrease of the interference which allow near-field interactions to be more visible. For the third harmonic ($n = 3$) the near-field interaction becomes even steeper.

Because the tip is periodically touching the sample, a nonsinusiodal distortion of the taping motion can be created by the mechanical motion. This leads to artifacts in the final microscopic image which are caused by the fact that the higher harmonics $n\Omega$ are excited also by

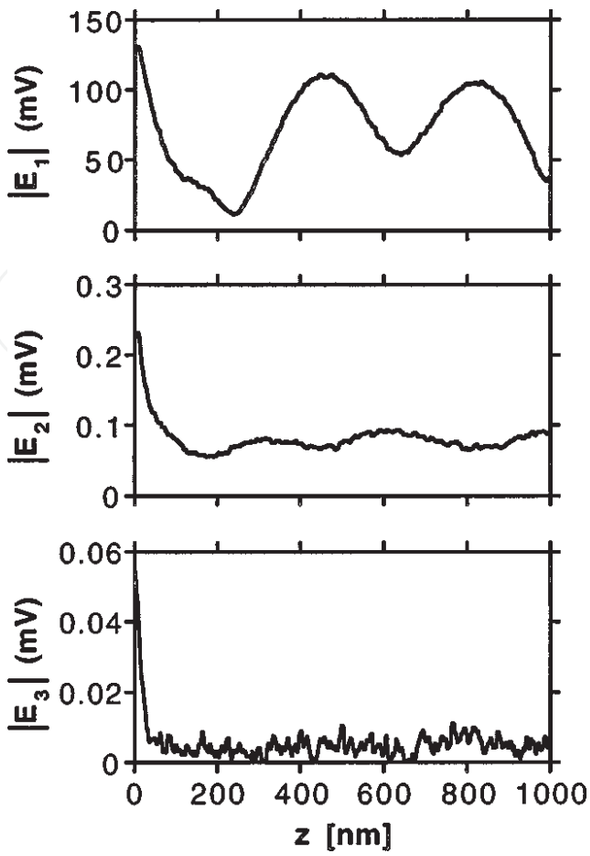


Fig. 5. Optical signal amplitude $|E_n|$ vs distance $z$ between tip and Au sample, for different harmonic demodulation orders $n$. ©2002 American Institute of Physics (Hillenbrand & Keilmann (2002))

mechanical motion. These mechanical harmonics cause direct modulations of the optical signals resulting in a distorted image. (Hillenbrand et al. (2000)) demonstrated that the artifacts depend on the sample and the tapping characteristics (such as amplitude, etc.). They have found that these mechanical artifacts are negligible for small $\Delta z < 50$nm and large setpoints $\Delta z/\Delta z_{free} > 0.9$.

In the mid-infrared region the appropriate illumination source was a $CO_2$ laser owing to its tunable properties from 9.2 to 11.2 $\mu m$. The attenuated laser beam of the power $\approx$ 10mW was focused by a Schwarzschild mirror objective (NA = 0.55) to the tip's apex. The polarization of the incident beam was, as in the previous case, optimized to have a large component in the direction of the tip shaft. This lead to a large enhancement of the near field interaction and increased the image contrast. The incident laser beam was split to create a reference which was reflected on a piezoelectrically controlled moveable mirror (Figure 4(b)). This mirror and the scattering tip created a Michelson interferometer. Using a homodyne detection the experimental setup was continuously switching the mirror between two positions. The first position corresponded to the maximum signal of the $n$-th harmonic at the lock-in amplifier (positive interference between the near-field scattered light and the reference beam) while the second position was moved by a $\lambda/8$ (90° shift of reference beam). With the experimental

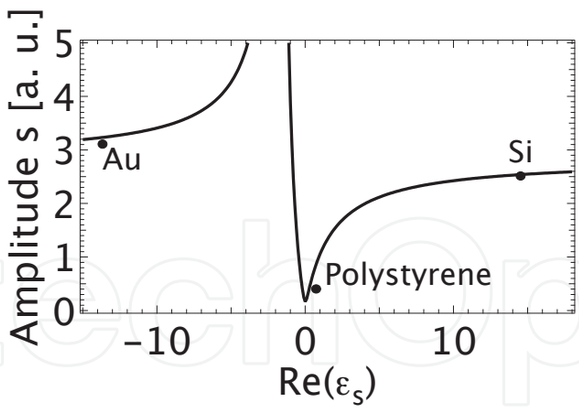


Fig. 6. Theoretically calculated the near-field scattering amplitude $s$ as a function of the real part of $\varepsilon_s$. The imaginary part of $\varepsilon_s$ was set to 0.1 and the tip was considered as Pt.

setup the detection of the amplitude and the phase of the near-field scattering was possible to detect, obtaining the near-field phase and amplitude contrast images. Further improvement of the background suppression was demonstrated by (Ocelic et al. (2006)) using a slightly modified homodyne detection with a sinusoidal phase modulation of the reference beam at frequency $M$ (see Figure 4(c)). This lead to the complete reduction of the background interference.

As we already mentioned and as is clearly visible from the equations described above, the near-field scattering depends on the dielectric function of the tip and the sample. We have calculated the amplitude of the near-field scattering as a function of the real part of $\varepsilon_s$ using Equation (3). The tip is assumed to be Pt ($\varepsilon_t = -5.2 + 16.7i$) and the sphere diameter $a = 20$nm. The result is depicted in Figure 6. The imaginary part of $\varepsilon_s$ was set to 0.1. The inserted dots represent the data for different materials at illumination wavelength $\lambda = 633$nm (Hillenbrand & Keilmann (2002)). As can be clearly seen from Figure 6, owing to different scattering amplitudes, a good contrast in the image of nanostructures consists of Au, Polystyrene and Si components should allow for easily observable images. Indeed, this was observed by (Hillenbrand & Keilmann (2002)) and is shown in Figure 7 . The AFM topography image itself can not distinguish between different materials. However, due to the material contrast, it is possible to observe different material structures in the s-SNOM image. This is consistent with the theoretical calculation in Figure 6. The lateral resolution of the s-SNOM image in Figure 7 is 10 nm.

### 2.2 Tip enhanced fluorescence microscopy

Owing to its sensitivity to single molecules and biochemical compositions, fluorescence microscopy is a powerful method for studying biological systems. There are various experimental setups of fluorescent microscopes that exceed the Rayleigh diffraction criterion which limits the practical spatial resolution to $\approx 250$nm. Recent modifications of conventional confocal microscopy, such as $4 - \pi$ (Hell & Stelzer (1992)) or stimulated emission depletion (Klar et al. (2001)) microscopies have pushed the resolution to tens of nanometers. Although these techniques offer a major improvement in the field of fluorescent microscopy, they require high power laser beams, specially prepared fluorophores and provide slow performance (not suitable for biological dynamics).

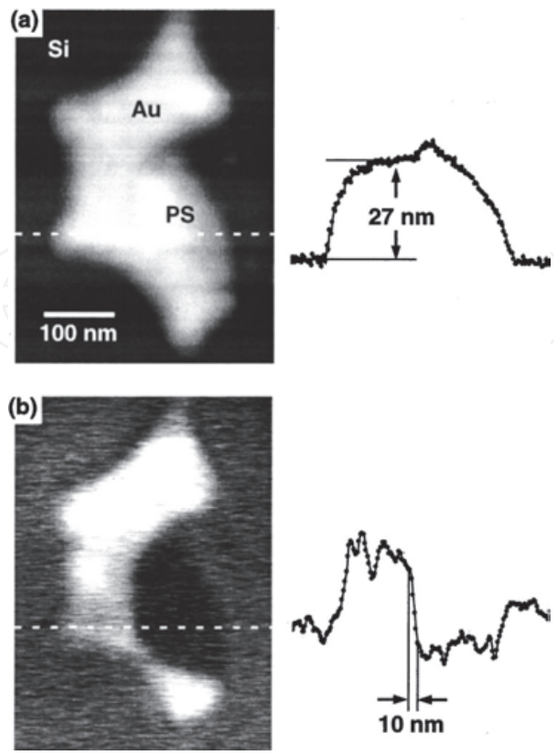


Fig. 7. Au island on Si observed in (a) topography, (b) optical amplitude $|E_3|$, with adjoining polystyrene particle. The line scans give evidence of purely optical contrast at 10 nm resolution, and of distinct near-field contrast levels for the three materials. ©2002 American Institute of Physics (Hillenbrand & Keilmann (2002))

Experimental setups of s-SNOM, as described in detail above, can be modified to sense fluorescence from nanoscale structures offering an alternative method to confocal microscopy. The near-field interaction between the sample and the tip causes the local increase of the one-photon fluorescence-excitation rate. The fluorescence is then detected by a single-photon sensitive avalanche photodiode. Such an experimental technique is called tip-enhanced fluorescence microscopy (TEFM) and its setup is schematically shown in Figure 8. There are two physical effects detected. The first one is an increase of detected fluorescence signal due to the near-field enhancement. The second one is the signal decrease due to the fluorescence quenching. These effects were demonstrated by various authors, for example by (Anger et al. (2006)). The fluorescence enhancement is proportional to the real part of the dielectric constant of the tip. On the other hand the fluorescence quenching is proportional to the imaginary part of the same dielectric function. Since these effects manifest themselves at short distances (bellow 20 nm), they can be used to obtain nanoscale resolution. Because the fluorescence enhancement leads to higher image contrast, silicon AFM tips are often used (due to their material parameters) for fluorescence studies of dense molecular systems.

In TEFM the illumination beam stimulates simultaneously a far-field fluorescence component $S_{ff}$, which is coming from direct excitation of fluorophores within the laser focus, and a near-field component $S_{nf}$, which is exited by a near-field enhancement. One can then define

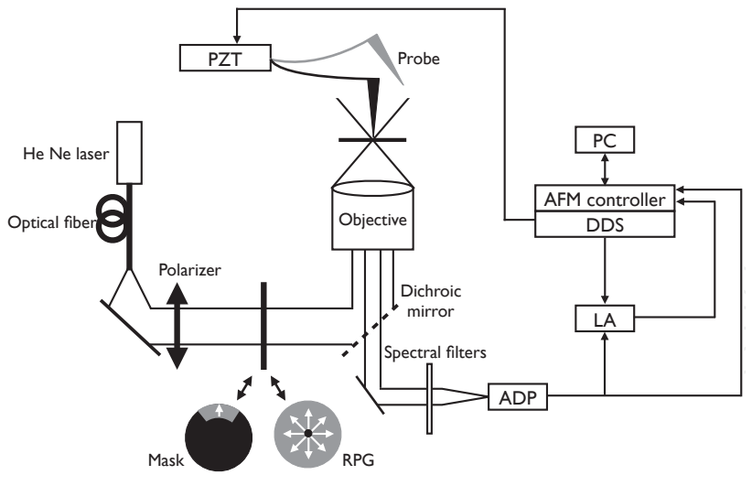


Fig. 8. Experimental setup of TEFM. RPG - radial polarization generator; PZT-piezoelectric transducer; ADP - avalanche photodiode; LA - lock-in amplifier; DDS - digital synthesizer.

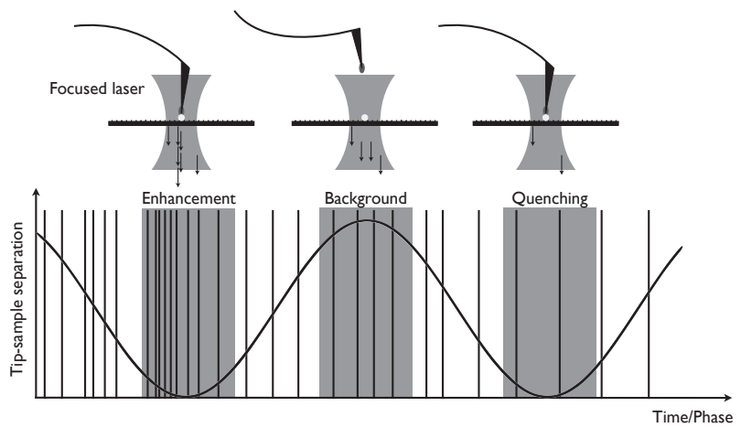


Fig. 9. Schematic picture of fluorescence modulation by AFM tip oscilation.

a contrast (C) of TEFM as

$$C = \frac{S_{nf}}{S_{ff}}. \tag{7}$$

Similarly to the s-SNOM setup it is possible to enhance the contrast and resolution of TEFM using a tapping mode in AFM and a demodulation algorithm for detected signal. Such process can be done by lock-in amplification. The scheme of the fluorescence modulation by an AFM tip oscillation is shown in Figure 9. When the tip is in the highest position above the sample no near-field interaction occurs. The detected signal is therefore coming from the background scattering excitation. If the tip is approaching the sample the fluorescence rate becomes maximally modified. The detected signal is either positive or negative depending on the fluorescence enhancement or quenching. TEFM example images of high density CdSe/ZnS quantum dots are shown in Figure 10. An improvement of the lateral resolution and contrast is clearly visible when using a TEFM with lock-in demodulation detection. The resolution of 10 nm, which is bellow the resolution of other fluorescence microscopies, demonstrates the main advantage of TEFM systems.

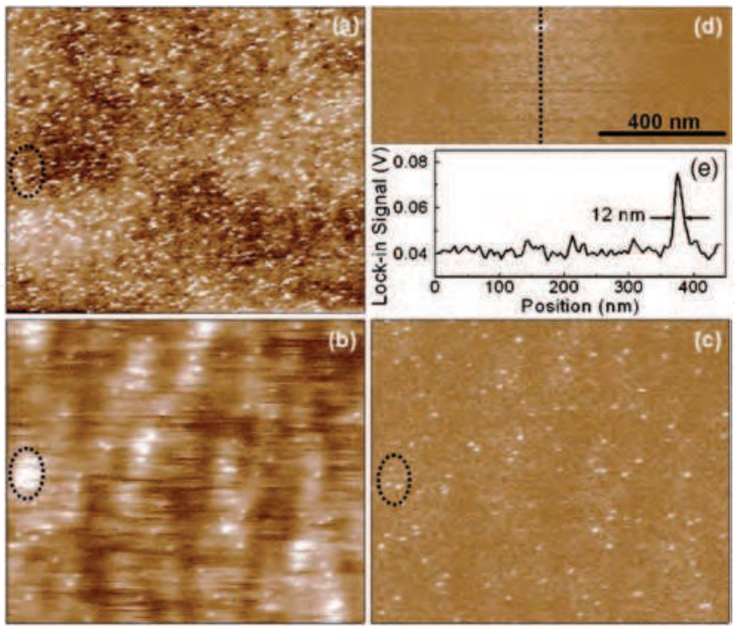


Fig. 10. High-resolution images of quantum dots. (a) AFM topography image; (b) photon-sum image; (c) TEFM image using lock-in demodulation. (a)–(c) are for a 5x5 $\mu m^2$ field of view. (d) TEFM image of a single quantum dot; (e) signal profile specified by the dotted line in (d). ©2006 American Institute of Physics (Xie et al. (2006))

## 3. AFM versus scatterometry

Recent advances of integrated circuits, including shortened dimensions, higher precision, and more complex shapes of geometric features patterned by modern lithographic methods, also requires higher precision of characterization techniques. This section briefly reviews some improvements of AFM and optical scatterometry, their comparison (with mutual advantages and disadvantages), and their possible cooperation in characterizing the quality of patterned nanostructures, especially in determining critical dimensions (CD), pattern shapes, linewidth roughness (LWR), or line edge roughness (LER).

### 3.1 AFM in the critical dimension (CD) mode with flared tips

It has been frequently demonstrated that accurate monitoring of sidewall features of patterned lines (or dots or holes) by AFM requires probe tips with special shapes and postprocessing algorithms to remove those shapes from the acquired images of the patterned profiles. A conventional AFM tip (with a conical, cylindrical, or intermediate shape) even with an infinitely small apex is only capable of detecting the surface roughness on horizontal surfaces (on the top of patterned elements or on the bottom of patterned grooves), but cannot precisely detect sidewall angles, LER, or particular fine sidewall features, as depicted in Fig. 11(a). Here the oscillation of the probe while scanning is only in the vertical direction so that the inverse profile of the tip is obtained instead of the correct sidewall shape. Only patterns with sidewall slopes smaller than the tip slopes (e.g., sinusoidal gratings) can be accurately detected after applying an appropriate image reconstruction transform such as the one shown by (Keller (1991)).

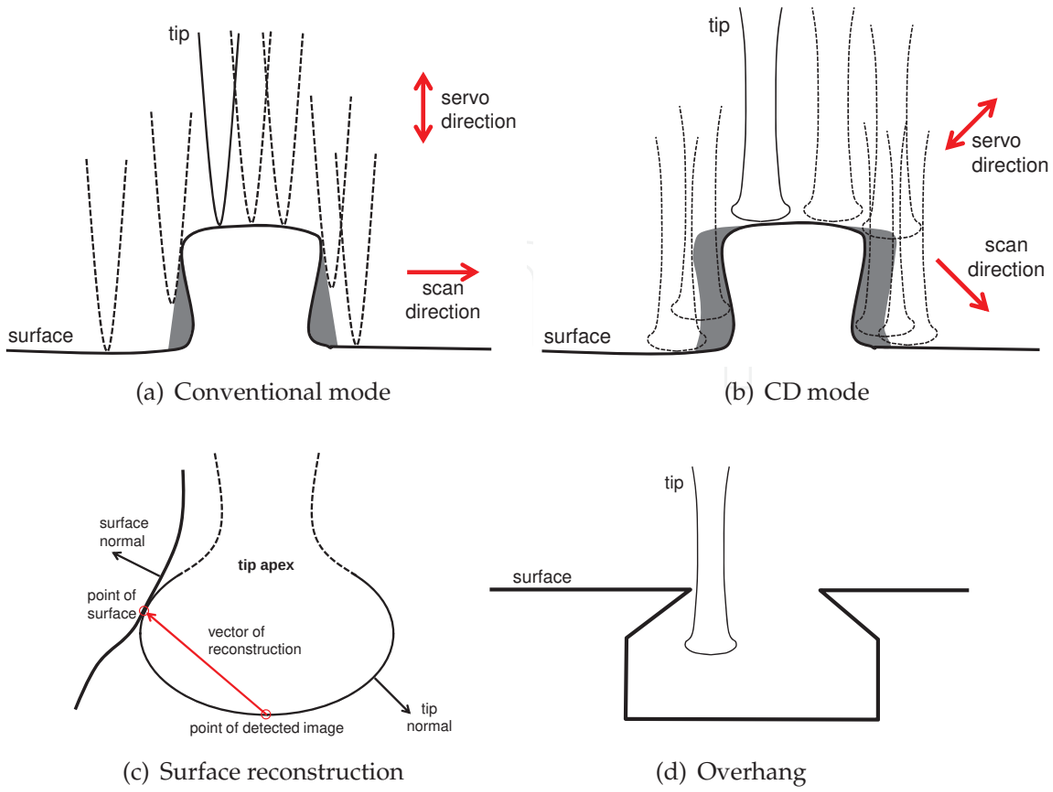


Fig. 11. AFM scanning of a patterned element in the conventional (a) and CD (b) modes with a conventional (a) and flared (b) tip apex. Postprocessing reconstruction of the surface uses the vector of reconstruction (c). The method can fail on overhang structures (d).

On the other hand, a CD tip, fabricated with a flared apex radius such as in (Liu et al. (2005)), can provide an accurate 3D patterned profile provided that it is applied in the CD mode. This mode, unlike the conventional deep trench mode where the tip only oscillates in the vertical direction, requires the tip to oscillate in both vertical and horizontal directions to follow the full surface topography for which multiple vertical points are possible for the same horizontal position, as depicted in Fig. 11(b). Analogously to conventional AFM scanning with a nonideal tip with a finite apex, the CD AFM scan also requires a postprocessing reconstruction of the real surface profile. An example of such a reconstruction, demonstrated by (Dahlen et al. (2005)), is the application of the reconstruction vector utilizing the fact that the normal to the surface is identical with the normal to the tip at each contact point, as displayed in Fig. 11(c). The method also utilizes algorithms of "reentrant" surface description.

The CD-AFM scanning can obviously fail for highly undercut surfaces for which the tip apex is not sufficiently flared, as visible in Fig. 11(d). However, such a structure can be advantageously used to carry out a topography measurement of the actual tip sidewall profile, as also described by (Dahlen et al. (2005)). Such a structure, designed solely for this reason, is called an overhang characterizing structure.

The advantages of the CD-AFM are that it is a nondestructive method (unlike cross-sectional SEM) which provides a direct image of the cross-sectional surface profile with relatively high

precision. However, the image becomes truly direct after an appropriate postprocessing procedure removing the tip influence. Moreover, some profile features cannot be revealed such as the precise shape of the top sharp corners, the exact vertical positions and radii of fine sidewall features, and—most importantly—the real shape of sharp bottom corners of the grooves.

### 3.2 AFM used for line edge roughness (LER) characterization

As the dimensions of patterned structures shorten to the nanometer scale, the LER and the LWR become important characteristics. Following (Thiault et al. (2005)), we briefly define the LER and LWR as follows:

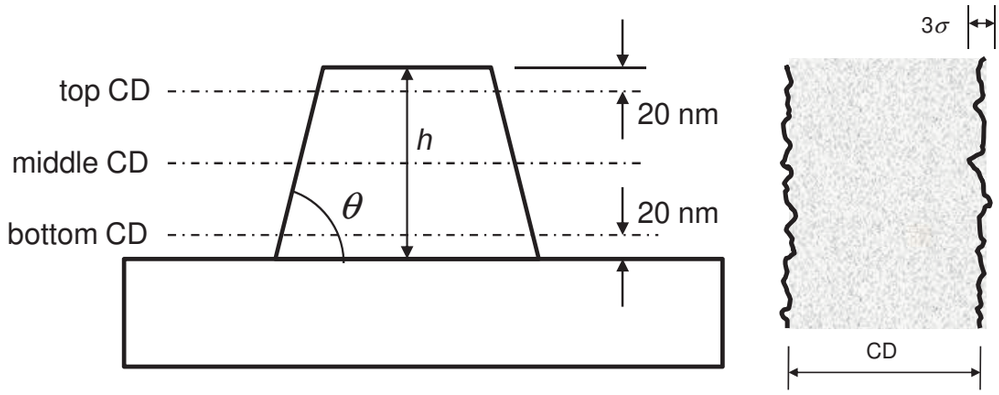


(a) Planes for measuring CD/LER (b) CD/LER

Fig. 12. Definitions of measuring CD and LER in different planes for AFM in the CD mode.

The LWR is defined as three standard deviations (denoted $3\sigma$) of the scanned linewidth variations at a height determined by the AFM user, while the CD represents the averaged value of the scanned dimension. Analogously, the LER is defined as its one-edge version, measured as three standard deviations of the variations from the straight line edge. Unfortunately, the CD-AFM scanning cannot accurately detect the linewidth at the very top and—especially—at the very bottom of the patterned grooves (which is due to the finite size of the tip apex). For this reason it is usually determined at some small height from the top (typically 20 nm, determined by the tip used), at the middle, and at some small height above the bottom (hence the top, middle, and bottom CD and LWR/LER, respectively). The corresponding planes are depicted in Fig. 12(a). The geometries for measuring the CD and the LER ($3\sigma$) at a chosen height are depicted in Fig. 12(b).

Although the LWR and LER at specified heights are also calculated from direct CD-AFM images, they can be affected by some further defects. As an example, consider a line whose both edges have equal LER values which are mutually uncorrelated. According to the statistical theory, $\sigma^2_{\mathrm{LWR}} = 2\sigma^2_{\mathrm{LER}}$ should be valid, so that the LWR should be $2^{1/2}$ times higher than the LER. However, (Thiault et al. (2005)) have shown that the stage drift (breaking the relative position of the tip and sample) during long-time measurement affect the LER considerably more than the LWR, because the time between the detection of two adjacent edges is much shorter than the time between two sequentional scans of the same edge.

### 3.3 Critical dimensions measured by scatterometry

Optical scatterometry, most often based on spectroscopic ellipsometry and sometimes combined with spectrophotometry (light intensity reflectance or transmittance), is an optical investigation method which combines optical measurements (typically in a wide spectral range, utilizing visible light with near ultraviolet and infrared edges) together with rigorous optical calculations. The spectra are calculated with varied input geometrical parameters of the patterned structure (optical CDs) and compared to the measured values to minimize the difference (optical error) as much as possible, employing the least square method for the optical error. The algorithm is usually referred to as the optical fitting procedure, and the obtained optical CDs are referred to as the optically fitted dimensions.

Various authors have presented the use of specular (0th-order diffracted) spectroscopic scatterometry to determine linewidths, periods, depths, and other fine profile features not accessible by AFM (such as the above mentioned bottom corners of grooves), as shown by (Huang & Terry Jr. (2004)). Obvious advantages of scatterometry is (besides non-destructiveness) higher sensitivity and no contact with any mechanical tool. Simply speaking, a photon examines the structure as it really stands and gives the true answer. Another advantage is the possibility to integrate an optical apparatus (most often a spectral ellipsometer) into a lithographer or deposition apparatus for the in situ monitoring of deposition and lithographic processes.

On the other hand, scatterometry has some disadvantages: Spectral measurements are indirect, and the measured spectra sometimes require very difficult analyses to reveal the real profile of the structure, which should be approximately known before starting the fitting procedure (to use it as an initial value). Moreover, the spectra can contain too many unknown parameters, or at least some vaguely known parameters. As an example, consider a grating made as periodic wires patterned from a Ta film deposited on a quartz substrate, which was optically investigated by (Antos et al. (2006)). The unknown parameters in the beginning were not only the geometrical dimensions and shape of the wires, but also the material properties of the Ta film, which were altogether correlated. Therefore, the first analysis was performed on a nonpatterned reference Ta film to determine the refractive index and extinction coefficient of Ta, as well as the thickness of the native oxide overlayer of $Ta_2O_5$. The obtained parameters were used as known constants within the second analysis, which was made on the Ta wire grating. This second analysis yielded the values of period, depth, linewidths, and the sidewall shape of the Ta wires. The sidewall shape was analytically approximated as paraboloidal, determined by two parameters: the top (smallest) linewidth (same as the bottom linewidth) and the middle (maximum) linewidth. Although the obtained geometry was revealed with higher precision than the geometry obtained by a direct method (unpublished SEM images in this case), all the obtained parameters were affected by a slight difference from the assumed paraboloidal sidewalls and by a native $Ta_2O_5$ overlayers that developed on the sidewalls (which were not taken into account in simulations). Each such difference or negligence from the real sample can contribute to discrepancy between the optical CDs and the real dimensions. Simply speaking, the advantage of high sensitivity can easily become a disadvantage, when the optical configuration is too sensitive to undesired features.

To illustrate the basic difference between conventional AFM and scatterometric measurements, consider a shallow rectangular grating patterned on the top of a 32-nm-thick

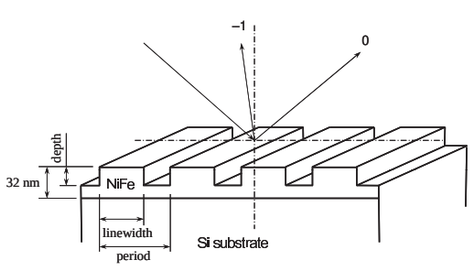


(a) Sample definition

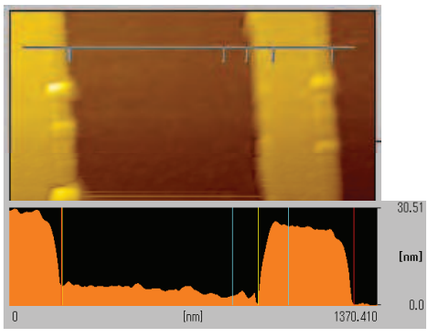


(b) AFM measurement

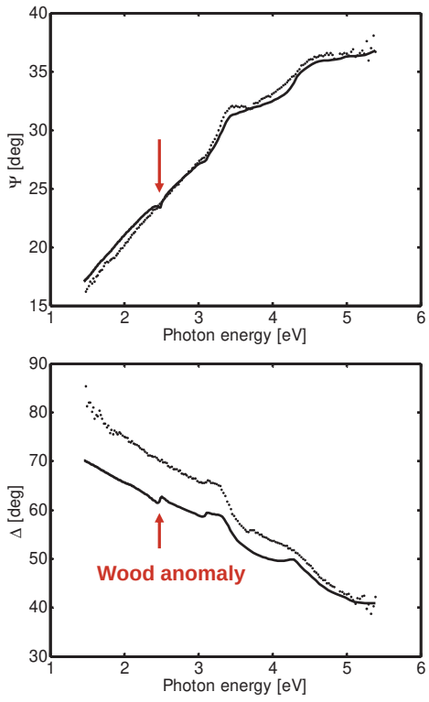


(c) Scatterometric fit

Fig. 13. Investigation of a sample (a) by AFM (b) and scatterometry (c).

Permalloy (NiFe) film deposited on a Si substrate, with geometry depicted in Fig. 13(a) and with more details in (Antos et al. (2005d)). The comparison of nominal geometrical parameters (those intended by the grating manufacturer) with parameters determined by AFM [Fig. 13(b)] and scatterometry [based on spectroscopic ellipsometry performed at three angles of incidence, 60, 70, and 80°, the last of which is displayed in Fig. 13(c)] is listed in Table 1.

| Parameter | nominal | AFM | scaled AFM | scatterometry |
|---|---|---|---|---|
| period | 1000 | 1091.5 | 1000⋆ | 1000⋆⋆ |
| linewidth | 500 | 359.4 | 329.3 | 307.2 |
| NiFe thickness | 32 | — | — | — |
| relief depth | 16 | 21.7 | 21.7 | 24.3 |

⋆fixed value

⋆⋆just verified from the position of the Wood anomaly

Table 1. Comparison of grating geometrical parameters obtained by AFM and scatterometry, together with nominal ones (intended by the manufacturer).

Here the AFM measurement provides a direct image of the grating's relief profile (for our purposes to scan a shallow relief the conventional-mode AFM is appropriate), but the horizontal values (period and linewidth) are affected by a wrong-scale error (9 %, which is quite high). According to our experiences, the period of patterns made by lithographic processes is always achieved with high precision, so that we scale the horizontal AFM parameters to obtain the nominal 1000 nm period and to keep the same period-to-linewidth

ratio (the verical depth is kept without change). The scaled AFM linewidth (329.3 nm, measured at the bottom) now corresponds well to the linewidth determined by scatterometry (307.2 nm); the 22 nm difference is probably due to the finite size of the apex of the AFM tip, which was previously explained in Fig. 11(a).

As visible in Fig. 13(c), the ellipsometric spectrum is not sensitive to the grating period, which is due to the shallow relief. For this reason the grating period could not be included in the fitting procedure. However, the period can be easily and with high precision verified by observing the spectral positions of Wood anomalies, which depend only on the period and the angle of incidence. In our case we observe the –1st-order Rayleigh wavelength (wavelength at which the –1st diffraction order becomes an evanescent wave) which provides precise verification of the nominal period of 1000 nm.

The 2.6 nm difference between the AFM and scatterometric values of the relief depth is difficult to explain. It might be again due the wrong vertical scale of the AFM measurement, or it might be due to some negligences of the used optical model such as the native top NiFe oxide overlayer or inaccurate NiFe optical parameters. Nevertheless, AFM and scatterometry differ from each other much less than how they differ from the nominal value, which indicates their adequacy. Finally, none of the methods were able to determine the full thickness of the deposited NiFe film (whose nominal value is 32 nm). While AFM was obviously disqualified in principle because it only detects the surface, optical scatterometry could provide this information if a reference sample (nonpatterned NiFe film simultaneously deposited on a transparent substrate) were investigated by energy transmittance measurement (again spectrally resolved for higher precision).

Another way to improve accuracy or the number of parameters to be resolved is to include higher diffraction orders in the analysis or to measure additional spectra such as magneto-optical spectroscopy (utilizing the magneto-optical anisotropy of NiFe). As an example, consider a grating made of Cr(2 nm)/NiFe(10 nm) periodic wires deposited on the top of a Si substrate. (Antos et al. (2005b)) used magneto-optical Kerr effect spectroscopy combining the analysis of the 0th and –1st diffraction order to determine the thicknesses of native oxide overlayers on the top of the Cr capping layer and on the top of Si substrate. It was shown that the 0th order of diffraction is more sensitive to features present both on wires and between them, whereas higher orders are more sensitive to differences between wires and grooves.

### 3.4 Line edge roughness determined by scatterometry

Besides measuring CDs, (Antos et al. (2005a)) have also shown that scatterometry is capable of evaluating the quality of patterning with respect to LER. Consider a pair of gratings similar to the one previously described, i.e., Cr(2 nm)/NiFe(10 nm) wires on the top of a Si substrate. AFM measurements of the two samples are shown in Fig. 14, where Sample 2 has obviously higher LER than Sample 1.

It is well known that *p*-polarized light is considerably more sensitive to surface features than *s*-polarized light. For this reason, magneto-optical Kerr effect spectroscopy in the –1st diffraction order was analyzed in a configuration where $r_{pp}$ (amplitude reflectance for the *p*-polarization) is close to zero. Since the Kerr rotation and ellipticity are approximately equal to the real and imaginary components of the complex ratio $r_{sp}/r_{pp}$ (here for the –1st order), they are very sensitive to the the wire edges. Fig. 15(a) displays experimental spectra

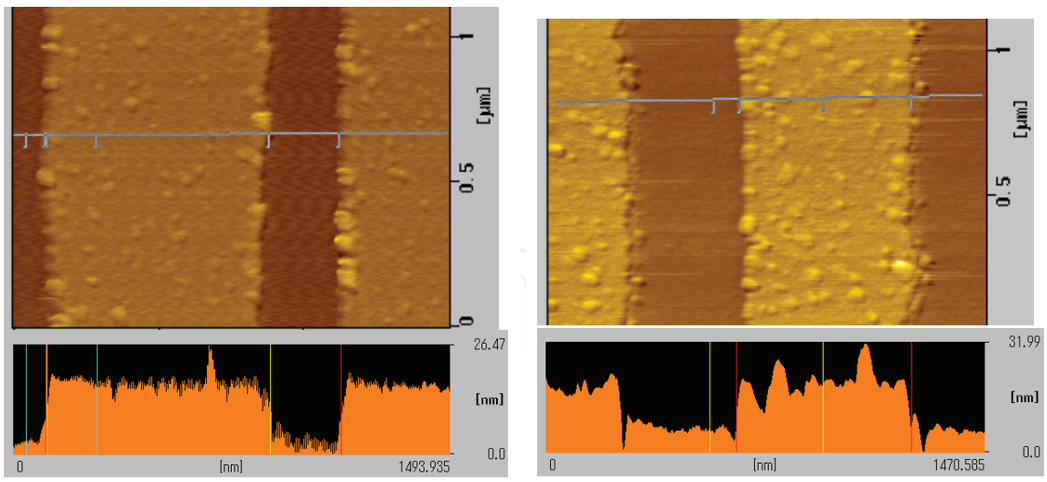


(a) Sample 1 (b) Sample 2

Fig. 14. AFM measurements of two Cr/NiFe wire samples with different LER.

measured on Sample 2 compared with two different models. First, the rigorous couple wave analysis (RCWA) is a rigorous method assuming diffraction on a perfect grating with ideal edges. Second, the local mode method (LMM) locally treats the grating structure as a uniform multilayer, neglecting thus the optical effect of the wire edges. Since none of the models corresponds well to the measured values, the reality is somewhere in the middle.

To include the effect of LER, we define a third model (optical LER method) as follows:

$$r_{pp}^{\mathrm{LER}} = r_{pp}^{\mathrm{LMM}} + \eta(r_{pp}^{\mathrm{RCWA}} - r_{pp}^{\mathrm{LMM}}) \tag{8}$$

where $r_{pp}^{\mathrm{LMM}}$ and $r_{pp}^{\mathrm{RCWA}}$ are reflectances calculated by the LMM and RCWA methods, and $\eta$ is a parameter whose values can be between zero and one. For the case $\eta = 1$ the sample behaves as a perfect grating with ideal edges ($r_{pp}^{\mathrm{LER}} = r_{pp}^{\mathrm{RCWA}}$), so that LER is zero. For the opposite case $\eta = 0$ the grating behaves as a random formation of islands with the wire structure, with their relative area equal to the grating filling factor, so that LER is infinite or at least higher than the linewidth. In reality the $\eta$ parameter will be somewhere in the middle and thus will provide the desired information about the LER. A fitting procedure carried on the two samples from Fig. 14 revealed the values of $\eta = 0.70$ for Sample 1 and $\eta = 0.53$ for Sample 2, which corresponds well to the obvious quality of the samples. The fitted spectra of the optical LER method are displayed in Fig. 15(b).

### 3.5 Joint AFM-scatterometry method

From the above comparisons, the mutual advantages and disadvantages of both AFM and scatterometry are obvious. For complex structures for which none of them can reveal all desired parameters when used solely, it is better to use them both. For instance, AFM can be used as the first method to determine the pattern shape and as many CDs as possible. Then, the obtained CDs are used as initial values for the optical fitting procedure in the frame of scatterometry, or some AFM parameters can be fixed (such as depth and top linewidth) and the remaining parameters can be fitted by scatterometry.

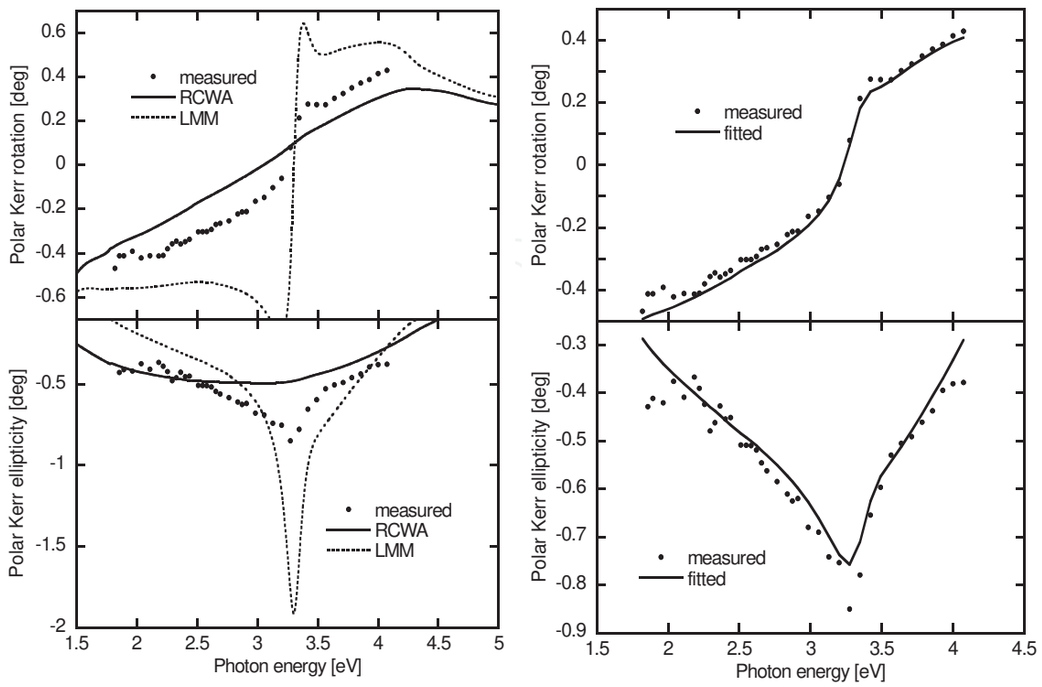


(a) Scatterometry using RCWA and LMM (b) Scatterometry including optical LER

Fig. 15. Experiment and modeling of MO spectroscopy in the $-1^{\text{st}}$ diffraction order with $p$-polarized incident light assuming a perfect grating (a) and including optical LER (b).

As an example, consider a nearly-sinusoidal surface-relief grating patterned on the top of a thick epoxy layer with a refractive index close to the index of glass on which the epoxy was deposited. A sample of such a structure was investigated by (Antos et al. (2005c)) to obtain the following results: First, a detailed AFM scan of the surface provided the precise shape of the relief function, being something between a sinusoidal and a triangular function,

$$f(x) = a\frac{d}{2}\sin\frac{2\pi x}{\Lambda} + (1-a)\frac{2d}{\Lambda}x, \tag{9}$$

where $a$ is a parameter of sharpness (the ratio between the sinusoidal and triangular shape), $d$ is the depth of the grating, and $\Lambda$ is its period. The AFM scan thus determined the period $\Lambda = 9365$ nm, depth of about $d = 700$ nm, and the parameter of sharpness $a = 0.6$. The period and the parameter of sharpness were then fixed as constants and used in a spectroscopic ellipsometry investigation to find more precisely the depth $d = 620$ nm and the values $\Delta n$ of how much the epoxy's refractive index differs from the index of the glass substrate.

## 4. Conclusion

In this chapter we have shown that AFM tips can be used effectively as near-field probes in near-field microscopy. Using a proper experimental setup one can resolve nanostructures down to 10 nm indenpendently of the illumination wavelength, which can be chosen between visible and infrared region.

AFM and optical applications were also reviewed with respect to measuring geometries and dimensions of laterally patterned nanostructures. Both AFM in the CD mode and scatterometry were capable of providing valuable information on periodic relief profiles with different mutual advantages and disadvantages.

## 5. Acknowledgement

This work is part of the research plan MSM 0021620834 financed by the Ministry of Education of the Czech Republic and was supported by the Grant Agency of the Czech Republic (no. P204/10/P346 and 202/09/P355) and a Marie Curie International Reintegration Grant (no. 224944) within the 7th European Community Framework Programme.

## 6. References

Anger, P., Bahradwaj, P. & Novotny, L. (2006). Enhancement and quenching of single-molecule fluorescence, *Phys. Rev. Lett.* Vol. 96(No. 11): 113002.

Antos, R., Mistrik, J., Yamaguchi, T., Visnovsky, S., Demokritov, S. O. & Hillebrands, B. (2005a). Evaluation of the quality of Permalloy gratings by diffracted magneto-optical spectroscopy, *Opt. Express* Vol. 13(No. 12): 4651–4656.

Antos, R., Mistrik, J., Yamaguchi, T., Visnovsky, S., Demokritov, S. O. & Hillebrands, B. (2005b). Evidence of native oxides on the capping and substrate of permalloy gratings by magneto-optical spectroscopy in the zeroth- and first-diffraction orders, *Appl. Phys. Lett.* Vol. 86(No. 23): 231101.

Antos, R., Ohlidal, I., Franta, D., Klapetek, P., Mistrik, J., Yamaguchi, T. & Visnovsky, S. (2005). Spectroscopic ellipsometry on sinusoidal surface-relief gratings, *Appl. Surf. Sci.* Vol. 244(No. 1-4): 221–224.

Antos, R., Pistora, J., Mistrik, J., Yamaguchi, T., Yamaguchi, S., Horie, M., Visnovsky, S. & Otani, Y. (2006). Convergence properties of critical dimension measurements by spectroscopic ellipsometry on gratings made of various materials, *J. Appl. Phys.* Vol. 100(No. 5): 054906.

Antos, R., Veis, M., Liskova, E., Aoyama, M., Hamrle, J., Kimura, T., Gustafik, P., Horie, M., Mistrik, J., Yamaguchi, T., Visnovsky, S. & Okamoto, N. (2005). Optical metrology of patterned magnetic structures: deep versus shallow gratings, *Proc. SPIE* Vol. 5752(No. 1-3): 1050–1059.

Cvitkovic, A., Ocelic, N. & Hillenbrand, R. (2007). Analytical model for quantitative prediction of material contrasts in scattering-type near-field optical microscopy, *Opt. Express* Vol. 15(No. 14): 8550.

Dahlen, G., Osborn, M., Okulan, N., Foreman, W., Chand, A. & Foucher, J. (2005). Tip characterization and surface reconstruction of complex structures with critical dimension atomic force microscopy, *J. Vac. Sci. Technol. B* Vol. 23(No. 6): 2297–2303.

Fee, M., Chu, S. & Hänsch, T. W. (1989). Scanning electromagnetic transmission line microscope with sub-wavelength resolution, *Optics Communications* Vol. 69(No. 3-4): 219–224.

Hecht, B. (1997). Facts and artifacts in near-field microscopy, *J. Appl. Phys.* Vol. 81(No. 6): 2492–2498.

Hell, S. W. & Stelzer, E. H. K. (1992). Fundamental improvement of resolution with a 4Pi-confocal fluorescence microscope using 2-photon excitation, *Opt. Commun.* Vol. 93(No. 5-6): 277–282.

Hillenbrand, R. & Keilmann, F. (2000). Complex optical constants on a subwavelength scale, *Phys. Rev. Lett.* Vol. 85(No. 14): 3029–3032.

Hillenbrand, R. & Keilmann, F. (2002). Material-specific mapping of metal/semiconductor/dielectric nanosystems at 10 nm resolution by backscattering near-field optical microscopy, *Appl. Phys. Lett.* Vol. 80(No. 1): 25–27.

Hillenbrand, R., Stark, M. & Guckenberger, R. (2000). Higher-harmonics generation in tapping-mode atomic-force microscopy: Insights into the tip-sample interaction, *Appl. Phys. Rev.* Vol. 76(No. 23): 3478–3480.

Huang, H.-T. & Terry Jr., F. L. (2004). Spectroscopic ellipsometry and reflectometry from gratings (Scatterometry) for critical dimension measurement and in situ, real-time process monitoring, *Thin Solid Films* Vol. 455-456(No. 1-2): 828–836.

Jackson, J. D. (1975). *Classical Electrodynamics*, John Wiley, New York.

Keilmann, F. & Hillenbrand, R. (2004). Near-field microscopy by elastic light scattering from a tip, *Phil. Trans. R. Soc. Lond. A* Vol. 362(No. 1817): 787–805.

Keller, D. (1991). Reconstruction of STM and AFM images distorted by finite-size tips, *Surf. Sci.* Vol. 253(No. 1-3): 353–364.

Klar, T. A., Engel, E. & Hell, S. W. (2001). Breaking Abbe's diffraction resolution limit in fluorescence microscopy with stimulated emission depletion beams of various shapes, *Phys. Rev. E* Vol. 64(No. 6): 066613.

Knoll, B. & Keilmann, F. (1999a). Mid-infrared scanning near-field optical microscope resolves 30 nm, *Journal of Microscopy* Vol. 194(No. 2-3): 512–515.

Knoll, B. & Keilmann, F. (1999b). Near-field probing of vibrational absorption for chemical microscopy, *Nature* Vol. 399(No. 6732): 134–137.

Liu, H., Klonowski, M., Kneeburg, D., Dahlen, G., Osborn, M. & Bao, T. (2005). Advanced atomic force microscopy probes: Wear resistant designs, *J. Vac. Sci. Technol. B* Vol. 23(No. 6): 3090–3093.

Mertz, J., Hipp, M., Mlynek, J. & Marti, O. (1994). Facts and artifacts in near-field microscopy, *Appl. Phys. Lett.* Vol. 81(No. 18): 2338–2340.

Novotny, L. & Hecht, B. (2006). *Principles of nano-optics*, Cambridge Univeristy Press, Cambridge.

Ocelic, N. & Hillenbrand, R. (2004). Subwavelength-scale tailoring of surface phonon polaritons by focused ion-beam implantation, *Nature Materials* Vol. 3(No. 9): 606–609.

Ocelic, N., Huber, A. & Hillenbrand, R. (2006). Pseudoheterodyne detection for background-free near-field spectroscopy, *Appl. Phys. Lett* Vol. 89(No. 10): 101124.

Porto, J. A., Carminati, R. & Greffet, J. J. (2000). Theory of electromagnetic field imaging and spectroscopy in scanning near-field optical microscopy, *J. Appl. Phys.* Vol. 88(No. 8): 4845–4850.

Thiault, J., Foucher, J., Tortai, J. H., Joubert, O., Landis, S., & Pauliac, S. (2005). Line edge roughness characterization with a three-dimensional atomic force microscope: Transfer during gate patterning processes, *J. Vac. Sci. Technol. B* Vol. 23(No. 6): 3075–3079.

Xie, C., Mu, C., Cox, J. R. & Gerton, J. M. (2006). Tip-enhanced fluorescence microscopy of high-density samples, *Appl. Phys. Lett.* Vol. 89: 143117.

Zayats, A. & Richards, D. (2009). *Nano-optics and near-field optical microscopy*, Artech House, Norwood.

Zenhausern, F., Martin, Y. & Wickramasinghe, H. K. (1995). Scanning interferometric apertureless microscopy: Optical imaging at 10 Angstrom resolution, *Science* Vol. 269(No. 5227): 1083–1085.

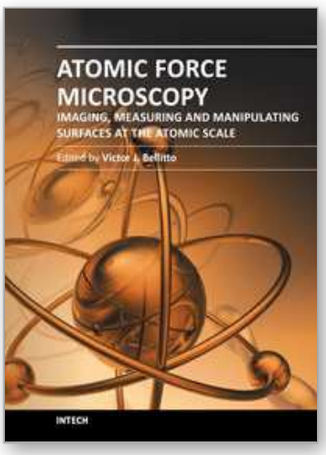


**Atomic Force Microscopy - Imaging, Measuring and Manipulating Surfaces at the Atomic Scale**

Edited by Dr. Victor Bellitto

ISBN 978-953-51-0414-8
Hard cover, 256 pages
**Publisher** InTech
**Published online** 23, March, 2012
**Published in print edition** March, 2012

With the advent of the atomic force microscope (AFM) came an extremely valuable analytical resource and technique useful for the qualitative and quantitative surface analysis with sub-nanometer resolution. In addition, samples studied with an AFM do not require any special pretreatments that may alter or damage the sample and permits a three dimensional investigation of the surface. This book presents a collection of current research from scientists throughout the world that employ atomic force microscopy in their investigations. The technique has become widely accepted and used in obtaining valuable data in a wide variety of fields. It is impressive to see how, in a short time period since its development in 1986, it has proliferated and found many uses throughout manufacturing, research and development.



**InTech Europe**
University Campus STeP Ri
Slavka Krautzeka 83/A
51000 Rijeka, Croatia
Phone: +385 (51) 770 447
Fax: +385 (51) 686 166
www.intechopen.com

**InTech China**
Unit 405, Office Block, Hotel Equatorial Shanghai
No.65, Yan An Road (West), Shanghai, 200040, China
中国上海市延安西路65号上海国际贵都大饭店办公楼405单元
Phone: +86-21-62489820
Fax: +86-21-62489821

IntechOpen